Drawdown of Atmospheric pCO2 via Dynamic Particle Export Stoichiometry in the Ocean Twilight Zone

Tatsuro Tanioka[1,1], Katsumi Matsumoto[1,1], and Michael William Lomas[2,2]

[1]University of Minnesota
[2]Bigelow Laboratory For Ocean Sciences

November 30, 2022

Abstract

The strength of the biological soft tissue pump in the ocean critically depends on how much organic carbon is produced via photosynthesis and how efficiently the carbon is transferred to the ocean interior. For a given amount of limiting nutrient, phosphate, soft tissue pump would be strengthened if the carbon (C) to phosphorus (P) ratio of sinking organic matter increases as the remineralization length scale of C increases. Here, we present a new data compilation of particle flux stoichiometry and show that C:P of sinking particulate organic matter (POM) in the ocean twilight zone on average is likely to be higher than the C:P ratio of surface suspended POM. We further demonstrate using a physics-biology coupled global ocean model combined with a theory from first principles that an increase in C:P export flux ratio in the ocean's twilight zone can lead to a considerable drawdown of atmospheric pCO2.

Drawdown of Atmospheric pCO_2 via Variable Particle Flux Stoichiometry in the Ocean Twilight Zone

Tatsuro Tanioka[1,2 *], Katsumi Matsumoto[1], and Michael W. Lomas[3]

[1] Department of Earth & Environmental Sciences, University of Minnesota, Minneapolis, MN, USA
[2] Department of Earth System Science, University of California Irvine, Irvine, CA, USA
[3] Bigelow Laboratory for Ocean Sciences, East Boothbay, ME, USA

**Correspondence to*: Tatsuro Tanioka (tatsurt@uci.edu)

Key Points:

- Global particle flux data suggests a systematic increase in carbon (C) to phosphorus (P) flux stoichiometry in the ocean twilight zone.
- Increase in the C:P export flux ratio through the twilight zone can substantially increase atmospheric pCO_2 drawdown.
- Further studies are required to elucidate mechanisms leading to spatiotemporal C:P export flux variability in the twilight zone.

Abstract

The strength of the biological soft tissue pump in the ocean critically depends on how much organic carbon is produced via photosynthesis and how efficiently the carbon is transferred to the ocean interior. For a given amount of limiting nutrient, phosphate, soft tissue pump would be strengthened if the carbon (C) to phosphorus (P) ratio of sinking organic matter increases as the remineralization length scale of C increases. Here, we present a new data compilation of particle flux stoichiometry and show that C:P of sinking particulate organic matter (POM) in the ocean twilight zone on average is likely to be higher than the C:P ratio of surface suspended POM. We further demonstrate using a physics-biology coupled global ocean model combined with a theory from first principles that an increase in C:P export flux ratio in the ocean's twilight zone can lead to a considerable drawdown of atmospheric pCO_2.

Plain Language Summary

The ocean's twilight zone, located below the ocean's sunlit zone, is a region where many critical biogeochemical processes occur but are not well characterized. Most notably, this is the zone where microbes and animals consume organic matter produced by primary producers in the surface ocean. How efficiently this organic matter is degraded exerts essential controls on atmospheric carbon dioxide levels and energy transfer in the marine food web. Here we show using a new global data compilation that organic carbon and phosphorus particles are degraded at different rates. This leads to a considerable change in carbon to phosphorus ratio at depth. We incorporate this variability into the 3D ocean model to show that such change can substantially increase the ocean's ability to absorb carbon dioxide from the atmosphere. The study ultimately highlights the need to accurately characterize the ocean's role in climate change by studying the particle dynamics in the twilight zone.

1. Introduction

The biological carbon pump is one of the critical mechanisms whereby marine phytoplankton convert inorganic carbon into organic carbon via photosynthesis, and that carbon is subsequently transported into the ocean interior (Sigman & Boyle, 2000). The conventional thinking is that oceanic carbon storage due to the biological carbon pump is proportional to the total inventory of phosphate in the interior ocean that arrived through the biological "regenerated" pathway (Ito & Follows, 2005; Marinov, Gnanadesikan, et al., 2008). This hypothesis assumes a fixed C:P stoichiometry, where carbon transfer efficiency into the ocean interior is tightly coupled to the transfer of phosphate from surface to depth. Under this framework, an increase in POM transfer efficiency and associated drawdown on atmospheric

pCO_2 will rapidly deplete surface nutrients, most notably in the North Atlantic and the Southern Ocean regions, where most deep water is formed (Sarmiento & Toggweiler, 1984).

Another school of thought proposes that the biological carbon pump can be strengthened if the C:P ratio of sinking POM increases with depth (Broecker, 1982a, 1982b; Knauer et al., 1979; Menzel & Ryther, 1964). This strengthening can happen if the remineralization length scale of particulate organic carbon (POC) is longer than that of particulate organic phosphorus (POP) such that C:P of the sinking POM exceeds C:P of upward inorganic flux (Christian et al., 1997). The seminal study by Menzel and Ryther (1964) demonstrated by sampling POM in the mesopelagic region of the Western North Atlantic that particulate phosphorus is remineralized more quickly than particulate carbon or nitrogen. Subsequent studies based on sediment traps and hydrographic studies have supported this theory (Knauer et al., 1979; J. H. Martin et al., 1987; Minster & Boulahdid, 1987). Furthermore, a recent inverse model study (Teng et al., 2014) argues that depth-dependent changes in C:P of sinking POM can better explain observed inorganic carbon and phosphate distributions than the model with fixed a C:P.

Here, we provide new lines of evidence for linking vertical variability in the C:P ratio of sinking POM in the twilight zone to carbon storage by using a compilation of recently published data and the time-series data from the Bermuda Atlantic Time-series Study (BATS). We then use a global ocean biogeochemistry model, combined with a theory derived from first principles, to illustrate that increases in the twilight zone C:P ratio could substantially strengthen the ocean biological carbon pump and drawdown of atmospheric CO_2. Previous modeling studies explored the impacts of remineralization length of particulate organic matter on atmospheric pCO_2, assuming fixed Redfield C:P stoichiometry throughout the entire water column (Kwon et al., 2009; Lauderdale & Cael, 2021; Matsumoto, 2007). The novelty of our 3D modeling study is that it investigates the effects of C:P changes both at the surface and in the subsurface ocean that also involve stoichiometric interaction between phytoplankton and zooplankton.

2. Methods

2.1 Data compilation of sinking POM

We compiled a new set of data on POC and POP export fluxes based on previous compilations by Antia (2005), Faul et al. (2005), and Paytan et al. (2003) to gather POC and POP sedimentary flux data that have been collected simultaneously. We have limited our analyses to open ocean samples and excluded coastal samples, and samples from the Southern Ocean as these sites are influenced mainly by resuspended or advected P (Faul et al.,

2005). Despite a wide range in sample treatment protocols, consistent trends across data indicate that the trends are not artifacts of sample processing or storage after collection (Faul et al., 2005).

We also included in our new data compilation several studies that were not included in the previous compilations (Benitez-Nelson et al., 2007; Engel et al., 2017; Grabowski et al., 2019; Karl et al., 2012; Lamborg et al., 2008; Lomas et al., 2010). As a quality control, we only include studies published after 2005 that report latitude and longitude information, and we took the average over the non-overlapping periods if multiple samples are taken from the same latitude and longitude. For brevity, we use the term PP (particulate phosphorus) to describe observed particulate phosphorus fluxes that do not separate particulate inorganic components from organic components. In addition, we limit our study to the samples below the epipelagic zone, operationally defined here as 100 m. Finally, for stations ALOHA and BATS, where multiple studies report sedimentary flux values, we selected the study by Grabowski et al. (2019) and Lomas et al. (2010) to represent the mean values for ALOHA and BATS, respectively. Selection processes based on the above criteria led to a total of 54 C:P flux ratio measurements (Table S1).

We note that of the total 54 measurements, 26 are collected by surface-tethered sediment traps, 25 by moored sediment traps, and 3 by neutrally buoyant free-drifting sediment traps (Table S1). All the surface-tethered samples are from the twilight zone (100 – 1000 m), and the majority of the moored sediment traps are from the deep ocean (> 1000 m). As the local hydrodynamic conditions, degree of solubilization, and the existence of zooplankton swimmers will impact collection bias differently for each sample (Antia, 2005; Buesseler et al., 2007), we report average values over the large geographic and the depth range to provide a broad picture of how C:P flux ratio changes with depth. Oceanographic regions (boundaries shown in Figure 1a) are based on the 0.3 mmol m^{-3} contour of the annually averaged PO_4 concentration from World Ocean Atlas 2018 (Garcia et al., 2018).

In addition to the time-averaged particle flux measurements, we present the continuous sedimentary flux timeseries measurements of POC and PP fluxes from BATS (31° 40’ N 064°10’W), collected from 2006 to 2019 at three different depths (150, 200, and 300 m). Using this data, we computed the Martin b exponent ($F(z) \propto (z/z_0)^{-b}$) for POC and PP separately for each time point using 150 m as a reference depth z_0. POC and PP sedimentary particle flux from the BATS station were measured using the standard method previously described (Lomas et al., 2010) and are publicly available (http://bats.bios.edu; last access April 23, 2021). All statistical analyses were conducted in R version 4.0.4 (R Core Team, 2021).

2.2 Ocean Biogeochemical Model

2.2.1 General Overview

We conducted all numerical simulations by applying the transport matrix model (TMM) (Khatiwala, 2007; Khatiwala et al., 2005) as an efficient offline method to simulate the 3D transport of tracers in the global ocean. The Transport Matrices (TMs) used in this study are derived from the circulation of the Estimating the Circulation and Climate of the Ocean (ECCO) project, with a horizontal resolution of 1° by 1° and 23 levels in the vertical (Stammer et al., 2004). ECCO circulation field is optimized to best fit hydrographic and remote sensing observations as well as the mean age of water parcels constrained by transient tracers (radiocarbon and chlorofluorocarbons, CFCs) (Khatiwala et al., 2012).

TMM circulation field is coupled to Model of Oceanic Pelagic Stoichiometry (MOPS), a simple NPZD model with nine default prognostic variables: phosphate, nitrate, dissolved inorganic carbon, alkalinity, oxygen, dissolved organic phosphorus, detritus, a single class of phytoplankton, and a single class of zooplankton (Kriest & Oschlies, 2015). In the original MOPS, the central currency of the model is phosphorus and assumes a fixed stoichiometric ratio of C:N:P:-O_2 = 117:16:1:151. Phytoplankton growth is limited by light and nutrients (phosphate and nitrate), assuming that the most limiting resource determines the growth rate. Phytoplankton is grazed by zooplankton as described a Holling Type III function with a quadratic dependence on phytoplankton biomass. The model assumes that a fixed fraction (15%) of egestion, zooplankton mortality, and phytoplankton loss is released as DOP, and the rest becomes detritus. Attenuation of detritus (POP) down the water column is described via the Martin Curve. A fraction of detritus that reaches the seafloor is buried instantaneously, and the non-buried fraction is resuspended back into the water column. The global river runoff equivalent to the annual flux of total organic P buried in the previous year is resupplied to the surface box to close the phosphorus budget (Kriest & Oschlies, 2013). The key biogeochemical parameters, including the Martin *b*, were objectively calibrated specifically for the ECCO transport matrix field to match observed PO_4, O_2, and NO_3 (Kriest et al., 2020; Figure S1).

2.2.2 Flexible C:P dynamics

This study added four new state variables related to organic carbon: phytoplankton carbon, zooplankton carbon, DOC, and detritus carbon (which we refer to as POC) to simulate the variable C:P ratio of organic matter. Phytoplankton P:C ratio in production layers is modeled using the power-law formulation as a function of ambient temperature and PO_4 (Tanioka & Matsumoto, 2017, 2020):

$$[P:C]_{PHY} = [P:C]_{PHY,ref} \cdot \left(\frac{[PO_4]}{[PO_4]_0}\right)^{s_{PO_4}^{P:C}} \cdot \left(\frac{T}{T_0}\right)^{s_T^{P:C}} \quad (1)$$

The exponents are the sensitivity factors determined by a meta-analysis (Tanioka and Matsumoto, 2020), and the subscript "0" indicates the reference environmental values, where at these values, P:C equals the reference P:C (i.e., $[P:C]_{PHY,ref}$ = Redfield Ratio = 1:117). The complete list of parameters used in the model is provided in Table S5.

Zooplankton P:C ratio is flexible and computed as a function of phytoplankton P:C in a power-law formulation:

$$[P:C]_{zoo} = [P:C]_{zoo,ref}{}^{1-H}[P:C]_{PHY}{}^{H} \quad (2)$$

where *H* is the homeostasis parameter, which takes a value of 0 when zooplankton P:C is completely homeostatic and a value of 1 when $[P:C]_{zoo}$ is directly proportional to $[P:C]_{PHY}$. In our study, we use *H* of 0.08 based on the meta-analysis by Persson et al. (2010) and assign the reference P:C of zooplankton, $[P:C]_{zoo,ref}$, equal to the Redfield ratio of 1:117. For zooplankton to maintain homeostatic C:P and cancel the mismatch between C:P of prey and themselves, zooplankton egests excess C into the environment as a new POC. Although studies suggest that 10-30% of POC ingested by zooplankton is released as DOC (Steinberg & Landry, 2017), we assume here for simplicity that all of the egested carbon goes to the POC pool.

For this study, we further assume that phytoplankton are always more C-rich than zooplankton (i.e., $[P:C]_{PHY} < [P:C]_{zoo}$) by setting hard-bound maximum $[P:C]_{PHY}$ to equal 1:117. With this simplification, zooplankton will only release excess C but not excess P. This ensures that the stoichiometry regulation of zooplankton will not affect values of inorganic nutrients and allows a fair comparison of model results across different sensitivity runs mentioned later. Some laboratory studies support our assumption that phytoplankton are more carbon-rich than zooplankton even under P-sufficient conditions (e.g., Boersma et al., 2009), and we believe that release of excess P by zooplankton occurs much less frequently than the release of excess C in most of the open ocean.

Kinetic parameters such as rate constants (λ) for remineralization for various source-minus-sink terms of POC and DOC are identical to those of POP and DOP, respectively. In the default run, the same Martin parameter (b = 1.46) is assigned to both POC and POP so that both elements have the same remineralization length scale and there is no preferential remineralization of one over the other. This default Martin *b* value of 1.46 is specifically

derived for MOPS by Kriest et al. (2020) to give the best fit toward hydrographic and satellite observations and is different from the original Martin *b* parameter of 0.86 (J. H. Martin et al., 1987). A full description of source-minus-sink terms of the ocean biogeochemistry model is given in Text S1.

2.2.3 Numerical experimental setup

We initialized MOPS for 3000 years under the constant climate scenario with fixed atmospheric pCO_2 at 280 ppm using monthly mean TMs, wind speed, temperature, salinity, and spatially variable P:C uptake ratios for phytoplankton and zooplankton following Equations (1) and (2) (Figure 1a, Figure S2). Following the 3000-year spin-up run, at which point the model has reached a steady state, we conducted sensitivity experiments to evaluate the response of the soft tissue pump to change in the C:P ratio of sinking POM. We systematically varied the Martin *b* parameter for POC (b_C) between 0.75 and 1.75 while keeping the Martin parameter for POP (b_P) constant at 1.46 to allow preferential remineralization of POP and POC over one another. This parameter range of b_C, while keeping b_P constant and applied to our model, brackets the global observed range in C:P flux at depth (Figure 1b). When b_C is smaller than the fixed b_P of 1.46, POP is preferentially remineralized over POC, and vice versa when b_C is greater than 1.46. Keeping the POP attenuation profile constant and not considering CO_2 radiative feedback across sensitivity runs ensures that the concentrations of all non-carbon tracers are identical in each sensitivity run. Oxygen demand during aerobic remineralization is computed from remineralization of organic phosphorus and not from organic carbon, with fixed stoichiometry; thus, oxygen utilization is kept identical in each run. This way, we can effectively isolate the effect of C:P on the strength of soft-tissue carbon pump without changing oxygen concentration and preformed and regenerated phosphate concentrations.

Following a 3000-year spin-up run, allowing all the chemical tracers to reach steady-state concentration, we conducted sensitivity runs with varying b_C for 1000 years to allow carbon-based tracers to reach new equilibrium states. CO_2 drift in the control run after 1000 years was -2.2 ppm, so we corrected for that deviation in each sensitivity run. The total amount of carbon in the ocean-atmosphere system remains constant as C:P of river supply and burial are fixed at 117, and phosphate inventory is steady. MOPS assumes OCMIP-type, gas exchange protocol with piston velocity and saturation derived from a monthly mean wind speed, salinity, and temperature derived from the MIT ECCO Ocean model and interpolated linearly onto the current time step (Kriest & Oschlies, 2015). In sensitivity experiments, we applied an infinitely fast gas exchange where surface ocean pCO_2 at each time step is in equilibrium with atmospheric pCO_2 to remove the effects of air-sea disequilibrium and reduce the time it takes for the system to reach a new equilibrium. In addition, alkalinity is kept spatially

uniform in all the sensitivity runs. These assumptions are essential for isolating the effects of the soft-tissue pump on atmospheric pCO_2 without complications caused by disequilibrium (Cliff et al., 2021; Khatiwala et al., 2019) and comparing model results with the theoretical predictions.

3. Results

3.1 Depth-dependent change in POC:POP flux ratio

Our new data compilation indicates that the C:P ratio of sinking POM in the twilight zone (100 – 1000 m) is generally higher than the regionally averaged C:P of suspended POM in the top 300 m in the overlying water column (Figure 1b). Observed C:P flux ratios in the twilight zone range between 83:1 and 500:1 with the global median of 294:1 (Table S2). This is approximately a factor of two greater than the global weighted mean C:P of suspended matter of 146:1 in the top 50 m (Martiny et al., 2013). Regionally, the tropical Atlantic exhibits the highest C:P flux ratio of 334:1 in the twilight zone, followed by the tropical Pacific (C:P = 318:1) and the Subtropical North Atlantic (C:P = 279:1). The Subpolar North Pacific region shows the lowest C:P flux ratio of 142:1 but is still higher than the mean surface suspended particle C:P of 94:1 in that region (Martiny et al., 2013, 2014). Two-way ANOVA shows that the geographic regions and the depth at which the samples are collected significantly affect the C:P flux ratio ($p < 0.05$; Table S3). C:P export flux ratio in the twilight zone measured by surface-tethered sediment traps are significantly elevated compared to C:P flux ratio measured in the deep ocean (> 1000 m) by moored sediment traps ($p < 0.05$). Our new data compilation confirms previous findings that the mean C:P flux ratio of sinking organic matter in the twilight zone is generally higher than the C:P of suspended POM (Knauer et al., 1979; Menzel & Ryther, 1964).

In addition to the global compilation, POM dynamics in the BATS ocean time-series provide continuous sedimentary POC and PP fluxes in the top mesopelagic depths (150 ~ 300 m) from 2006 to 2019. Median Martin *b* is significantly higher for PP ($b_P = 1.28$) compared to POC ($b_C = 0.98$), which indicates a shallower remineralization profile of PP over POC (Figure 2b, Table S4). There were no temporal shifts in the magnitude of Martin *b* for PP and POC between 2006 and 2019, but the systematic difference in Martin *b* for PP and POC at BATS is persistent over time (Figure 2a), indicating that preferential remineralization of PP over POC is a prevalent feature in the subtropical region.

3.2 Effects of variable C:P export stoichiometry on pCO_2: Theory and Model Results

Following the first-principle argument (Ito & Follows, 2005; Marinov, Follows, et al., 2008; Marinov, Gnanadesikan, et al., 2008), the total ocean carbon storage due to soft-tissue pump

(OCS_{soft}) can be determined by the remineralized PO_4 inventory ($\overline{PO_{4remin}}$) scaled by a global mean C:P ratio of remineralization ($r_{C:P}$):

$$OCS_{soft} = r_{C:P} \cdot \overline{PO_{4remin}} \cdot V_{oc} = r_{C:P} \cdot (\overline{PO_4} - \overline{PO_{4pref}}) \cdot V_{oc} \quad (3)$$

where V_{OC} is the ocean volume, and $\overline{PO_4}$ (= 2.14 mmol m^{-3}) and $\overline{PO_{4pref}}$ (= 1.09 mmol m^{-3}) are global volume averages for total PO_4 and preformed PO_4, respectively obtained from our MOPS-ECCO model simulation at steady state. Preformed PO_4 in the ocean interior in model simulations is computed from AOU and fixed -O_2:P of 151.1. Our modeled mean PO_4 compares well with observed global mean PO_4 of 2.26 mmol m^{-3}, and mean observed preformed PO_4 concentrations of 2.2 mmol m^{-3} and 0.8 mmol m^{-3} for Antarctic Bottom Water (AABW) and North Atlantic Deepwater (NADW), respectively (Duteil et al., 2012).

Atmospheric pCO_{2a} can be related to global mean C:P assuming constant phosphate inventory, total buffered carbon in the ocean ($C_{buffered}$), and pCO_2 when OCS_{soft} is zero ($c_1 = 651$ ppm):

$$pCO_{2a} \cong c_1 \cdot e^{-\frac{OCS_{soft}}{C_{buffered}}} = c_1 \cdot e^{-\frac{r_{C:P} \cdot (\overline{PO_4} - \overline{PO_{4pref}}) \cdot V_{oc}}{C_{buffered}}} \quad (4)$$

The definition of "buffered carbon" ($C_{buffered}$) follows that of previous studies (Goodwin et al., 2007; Marinov, Follows, et al., 2008; Marinov, Gnanadesikan, et al., 2008):

$$C_{buffered} = M_a \cdot pCO_{2a} + V_{oc} \cdot \overline{DIC_{eq}}/R \cong \text{constant}$$

where M_a is the mass of the atmosphere, R is the Revelle buffer factor, and $\overline{DIC_{eq}}$ is the globally averaged surface equilibrium DIC (Table S6).

We posit that the global mean C:P of remineralization ($r_{C:P}$) can be predicted as the ratio between the globally integrated flux of POC and POP in the twilight zone:

$$r_{C:P} \cong \frac{\int_{z_o}^{z'} F_{C,0} \left(\frac{z}{z_o}\right)^{-b_C} dz}{\int_{z_o}^{z'} F_{P,0} \left(\frac{z}{z_o}\right)^{-b_P} dz} = r_{C:P}(z_0) \cdot \frac{\int_{z_o}^{z'} \left(\frac{z}{z_o}\right)^{-b_C} dz}{\int_{z_o}^{z'} \left(\frac{z}{z_o}\right)^{-b_P} dz} \quad (5)$$

where $r_{C:P}(z_0)$ is the global mean C:P of NPP in the euphotic zone at depth z_0; b_P and b_C are Martin's b exponent for POP and POC, respectively, and z' is the bottom of the depth of the twilight zone. For theoretical prediction of the global mean $r_{C:P}$ from Equation (5), we used fixed surface reference depth z_0 of 100 m and tested different mesopelagic depth horizons z' (250, 1000, and 2000 m). We compared true OCS_{soft} and $pCO2_a$ from the model output with the theoretical predictions based on Equations (3) – (5) and assessed how well $r_{C:P}$ could be estimated from the Martin b parameters alone.

Figure 3a illustrates the relationship between $r_{C:P}$ and the strength of the soft-tissue pump measured by the total ocean carbon storage due to soft-tissue pump, OCS_{soft}, at steady-state. Each steady state model results with different values of b_C are shown as individual points with different colors. Theoretical predictions with different mesopelagic depth horizons z' are shown with lines, and the depth selection z' of 1000 m best matches the model results. A good agreement between the model result and theory gives us confidence that much of the change in $r_{C:P}$ can be explained by preferential remineralization of POP over POC occurring in the twilight zone (between 100 - 1000 m) and not in the epipelagic or bathypelagic regions of the ocean.

Our model results suggest that $r_{C:P}$ can change the strength of ocean soft-tissue pump and atmospheric CO_2 drawdown in two ways. First is via a change in the surface C:P ratio, $r_{C:P}(z_0)$, and this effect can be visualized by comparing the model output with fixed C:P ("Redfield") and the "Default ($b_c = b_p$)" run with variable C:P at the surface but no preferential remineralization at depth. Incorporating variable surface C:P can increase carbon export at 100 m by 3.0 PgC yr^{-1} compared to the Redfield run and increase the total carbon storage by 422 PgC or 21% (Table S6). It is important to note that this mechanism implicitly assumes that small cells are exported more efficiently if the increase in C:P of phytoplankton is tied to the reduction in the weighted size of the phytoplankton.

The second effect for strengthening soft-tissue pump is via an increase in the remineralization length scale of POC by reducing b_C relative to b_P. The global mean C:P remineralization ratio, $r_{C:P}$, increases from 142 in the default run with no preferential remineralization to as high as 309 when b_C is roughly halved from 1.46 to 0.75. Halving b_C in the model decreases pCO_2 by ~180 ppm from 305 ppm to 128 ppm and more than doubles the carbon storage by the soft-tissue pump. There is a range of 100 ppm given the large spread in b_C required to explain the observed C:P of POM flux (Figure 1), and the real-world range of pCO_2 remains difficult to be constrained in the current study. However, our sensitivity model runs indicate the potential of particle flux stoichiometry to significantly perturb the global carbon cycle.

An increase in the particle $r_{C:P}$ in the twilight zone and the subsequent strengthening of soft-tissue carbon pump leads to reduction of DIC in the surface and more DIC sequestration in the mid to deep ocean (Figure S3). In the "Default" model run with variable C:P at the surface but with no change in C:P at depth, ΔDIC from the Redfield run is mainly limited in the top 1000 m, and the carbon sequestration signal does not penetrate to the deep ocean (Figure S3c, d). However, when we allow the depth-dependent increase in POC:POP flux via assigning the lower value of b_C, the signal of variable stoichiometry can potentially readily reach the deep ocean. The largest DIC increase occurs in the deep North Pacific Ocean, reflecting the greater accumulation of respired carbon along the deep branch of the overturning circulation (Figure S3e, f). Accumulation of DIC in the deep Pacific is accompanied by a considerable reduction of DIC concentration in the surface ocean and NADW, which is indicative of the subduction of the DIC deplete surface water transported poleward.

4. Discussion and Outlook

Our data compilation suggests that, on average, particulate organic carbon has a longer remineralization length scale than particulate phosphorus, thus leading to an increased C:P export flux ratio with depth in the twilight zone. However, we do not currently have a good understanding of the mechanisms that lead to such stoichiometric variability. Previous studies (Broecker, 1982b, 1982a; Wakeham et al., 1984) speculated that decoupling of POC and POP remineralization could occur in three steps: (1) selective removal of the more labile organic matter fractions during the digestive process of zooplankton, (2) formation of fecal pellets enriched with non-labile organic matter such as fiber, and (3) consolidation of fragmented sloppy feeding material and fecal material into larger sinking particles. When food quality is low (i.e., high C:P of prey), zooplankton retains nutritive elements such as P and N while releasing crude fiber carbon behind as feces leading to high C:P of fecal pellets (Steinberg & Landry, 2017). These mechanisms provide plausible reasons for a larger positive deviation of C:P of sinking POM relative to surface suspended POM in the oligotrophic regions (e.g., Subtropical North Pacific) compared to more nutrient-rich regions (e.g., Subpolar North Pacific).

Microbial transformation of sinking particles can further give rise to C:P in the twilight zone if microbes attached to the particles preferentially remineralize P over C (Karl et al., 1996; Taylor et al., 1986). However, the biochemical mechanisms for preferential remineralization of POM by heterotrophic microbes are somewhat more uncertain than dissolved organic matter (DOM) because the biochemical compositions of DOM and POM are quite different (Loh & Bauer, 2000; Paytan et al., 2003). Although preferential removal of different types of particulate organic phosphorus compounds, such as phosphonates relative to phosphoesters,

have been observed (Benitez-Nelson et al., 2004), and bacteria are known to have a greater tendency for consuming P than C from their food substrates (Gundersen et al., 2002), we do not currently have a good understanding of mechanisms how bacteria attached to sinking POM can preferentially remineralize P over C (Benitez-Nelson, 2000).

Physical mechanisms such as abiotic particle fragmentation that physically removes P may also increase the C:P flux ratio at depth. It has been suggested that the smaller, older refractory particles that have undergone more fragmentation contribute a greater fraction of POM collected in the deeper trap samples because smaller particles generally have a longer residence time in the oceans (Karl et al., 1988; Wakeham et al., 1984). Physical mixing and circulation are also likely to be vital in explaining why C:P flux ratios do not continue to increase indefinitely below the twilight zone. As nutrient concentrations in the deep ocean (> 400 m) show that the globally averaged bulk of organic matter remineralization occurs in approximately Redfield ratio (Anderson & Sarmiento, 1994), the physical mechanisms maybe playing critical roles in averaging the signal of elevated POC:POP in the surface and twilight zone from reaching the deep ocean (Shaffer et al., 1999; Weber & Deutsch, 2010).

Methodological issues related to sediment traps, including hydrodynamic biases, swimmers, and solubilization, prohibit us from making firm quantitative conclusions on the extent of selective remineralization of POP over POC at different oceanographic regions (Buesseler, Antia, et al., 2007). A previous study showed that solubilization of P after being collected in the sediment traps occurs at a much greater extent relative to C and could change the estimation of the stoichiometric C:P ratios of sinking particles (Antia, 2005; Buesseler et al., 2007). However, enhanced remineralization and solubilization of P, relative to C, whether it occurs in the water column or in the sediment trap, support our point that P is more labile than C.

Here, we showed using a 3D model and theory that C:P variability in the twilight zone can modulate the strength of carbon sequestration by at least 20%. Our result is unique in that redistribution of DIC can occur without a change in the nutrient distribution, and the change in DIC distribution is entirely through the change in particle export stoichiometry. Ocean biogeochemical models are beginning to incorporate flexible C:N:P of phytoplankton (Chien et al., 2020; Kwiatkowski et al., 2018; Matsumoto et al., 2021; Pahlow et al., 2020) but most models do not yet explicitly consider a change in the elemental stoichiometry of POM once it leaves below the euphotic zone. In this regard, other mathematical forms of remineralization profiles such as exponential function (Armstrong et al., 2001; Lauderdale & Cael, 2021; Pavia et al., 2019) to prevent flux stoichiometry from increasing indefinitely with depth. In addition to modeling passive fluxes, models also need to consider active transport of material

via vertically migrating animals and how they change C:N:P flux stoichiometry in the twilight zone (Hannides et al., 2009; Saba et al., 2021; Schiettekatte et al., 2020). As many biogeochemical processes in the ocean twilight zone that govern particle transfer are still enigmatic (Boyd et al., 2019; Robinson et al., 2010), future studies using new technologies such as Underwater Vision Profilers, robots, and autonomous Argo floats could significantly advance our current understanding of particle dynamics in the twilight zone (A. Martin et al., 2020).

Acknowledgments

This study was supported by the U.S. National Science Foundation (OCE-1827948). In addition, TT acknowledges support from the Simons Foundation Postdoctoral Fellowships in Marine Microbial Ecology (Award 724483). We thank Samar Khatiwala for providing technical support on TMM and Iris Kriest for scripts to analyze the model output. Numerical modeling and analysis were carried out using resources at the University of Minnesota Supercomputing Institute. Ocean biogeochemical model codes are available in the author's GitHub (https://github.com/tanio003/tmm/tree/TT_Release) and are archived in Zenodo (http://doi.org/10.5281/zenodo.4960404). Model input and output files are publicly archived in Dryad (https://doi.org/10.5061/dryad.70rxwdbxq). The authors acknowledge and thank the numerous principal investigators, researchers, and technicians who have contributed to the BATS time-series since its inception, and the continued support of BATS by NSF through the current (OCE-1756054) and previous awards.

Reference:

Anderson, L. A., & Sarmiento, J. L. (1994). Redfield ratios of remineralization determined by nutrient data analysis. *Global Biogeochemical Cycles*, *8*(1), 65–80. https://doi.org/10.1029/93GB03318

Antia, A. N. (2005). Solubilization of particles in sediment traps: revising the stoichiometry of mixed layer export. *Biogeosciences*, *2*(2), 189–204. https://doi.org/10.5194/bg-2-189-2005

Armstrong, R. A., Lee, C., Hedges, J. I., Honjo, S., & Wakeham, S. G. (2001). A new, mechanistic model for organic carbon fluxes in the ocean based on the quantitative association of POC with ballast minerals. *Deep-Sea Research Part II: Topical Studies in Oceanography*, *49*(1–3), 219–236. https://doi.org/10.1016/S0967-0645(01)00101-1

Benitez-Nelson, C. R. (2000). The biogeochemical cycling of phosphorus in marine systems. *Earth-Science Reviews*, *51*(1–4), 109–135. https://doi.org/10.1016/S0012-8252(00)00018-0

Benitez-Nelson, C. R., O'Neill, L., Kolowith, L. C., Pellechia, P., & Thunell, R. (2004). Phosphonates and particulate organic phosphorus cycling in an anoxic marine basin. *Limnology and Oceanography*, *49*(5), 1593–1604. https://doi.org/10.4319/lo.2004.49.5.1593

Benitez-Nelson, C. R., O'Neill Madden, L. P., Styles, R. M., Thunell, R. C., & Astor, Y. (2007). Inorganic and organic sinking particulate phosphorus fluxes across the oxic/anoxic water column of Cariaco Basin, Venezuela. *Marine Chemistry*, *105*(1–2), 90–100. https://doi.org/10.1016/j.marchem.2007.01.007

Boersma, M., Becker, C., Malzahn, A. M., & Vernooij, S. (2009). Food chain effects of nutrient limitation in primary producers. *Marine and Freshwater Research*, *60*(10), 983–989. https://doi.org/10.1071/MF08240

Boyd, P. W., Claustre, H., Levy, M., Siegel, D. A., & Weber, T. S. (2019). Multi-faceted particle pumps drive carbon sequestration in the ocean. *Nature*, *568*(7752), 327–335. https://doi.org/10.1038/s41586-019-1098-2

Broecker, W. S. (1982a). Glacial to interglacial changes in ocean chemistry. *Progress in Oceanography*, *11*(2), 151–197. https://doi.org/10.1016/0079-6611(82)90007-6

Broecker, W. S. (1982b). Ocean chemistry during glacial time. *Geochimica et Cosmochimica Acta*, *46*(10), 1689–1705. https://doi.org/10.1016/0016-7037(82)90110-7

Buesseler, K. O., Antia, A. N., Chen, M., Fowler, S. W., Gardner, W. D., Gustafsson, O., et al. (2007). An assessment of the use of sediment traps for estimating upper ocean particle fluxes. *Journal of Marine Research*, *65*(3), 345–416. https://doi.org/10.1357/002224007781567621

Chien, C.-T., Pahlow, M., Schartau, M., & Oschlies, A. (2020). Optimality-based non-Redfield plankton-ecosystem model (OPEM v1.1) in UVic-ESCM 2.9 - Part 2: Sensitivity analysis and model calibration. *Geoscientific Model Development*, *13*(10), 4691–4712. https://doi.org/10.5194/gmd-13-4691-2020

Christian, J. R., Lewis, M. R., & Karl, D. M. (1997). Vertical fluxes of carbon, nitrogen, and phosphorus in the North Pacific Subtropical Gyre near Hawaii. *Journal of Geophysical Research: Oceans*, *102*(C7), 15667–15677. https://doi.org/10.1029/97JC00369

Cliff, E., Khatiwala, S., & Schmittner, A. (2021). Glacial deep ocean deoxygenation driven by biologically mediated air–sea disequilibrium. *Nature Geoscience*, *14*(1), 43–50. https://doi.org/10.1038/s41561-020-00667-z

Duteil, O., Koeve, W., Oschlies, A., Aumont, O., Bianchi, D., Bopp, L., et al. (2012). Preformed and regenerated phosphate in ocean general circulation models: can right total concentrations be wrong? *Biogeosciences*, *9*(5), 1797–1807. https://doi.org/10.5194/bg-9-1797-2012

Engel, A., Wagner, H., Le Moigne, F. A. C., & Wilson, S. T. (2017). Particle export fluxes to the oxygen minimum zone of the eastern tropical North Atlantic. *Biogeosciences*, *14*(7), 1825–1838. https://doi.org/10.5194/bg-14-1825-2017

Faul, K. L., Paytan, A., & Delaney, M. L. (2005). Phosphorus distribution in sinking oceanic particulate matter. *Marine Chemistry*, *97*(3–4), 307–333. https://doi.org/10.1016/j.marchem.2005.04.002

Garcia, H., Weathers, K. W., Paver, C. R., Smolyar, I., Boyer, T. P., Locarnini, R. A., et al. (2018). World Ocean Atlas 2018. Volume 4: Dissolved Inorganic Nutrients (phosphate, nitrate and nitrate+nitrite, silicate). In A. Mishonov (Ed.), *NOAA Atlas NESDIS 84* (Vol. 84, p. 35).

Goodwin, P., Williams, R. G., Follows, M. J., & Dutkiewicz, S. (2007). Ocean-atmosphere partitioning of anthropogenic carbon dioxide on centennial timescales. *Global Biogeochemical Cycles*, *21*(1), 1–10. https://doi.org/10.1029/2006GB002810

Grabowski, E., Letelier, R. M., Laws, E. A., & Karl, D. M. (2019). Coupling carbon and energy fluxes in the North Pacific Subtropical Gyre. *Nature Communications*, *10*(1), 1895. https://doi.org/10.1038/s41467-019-09772-z

Gundersen, K., Heldal, M., Norland, S., Purdie, D. A., & Knap, A. H. (2002). Elemental C, N, and P cell content of individual bacteria collected at the Bermuda Atlantic Time-series Study (BATS) site. *Limnology and Oceanography*, *47*(5), 1525–1530. https://doi.org/10.4319/lo.2002.47.5.1525

Hannides, C. C. S., Landry, M. R., Benitez-Nelson, C. R., Styles, R. M., Montoya, J. P., & Karl, D. M. (2009). Export stoichiometry and migrant-mediated flux of phosphorus in the North Pacific Subtropical Gyre. *Deep-Sea Research Part I: Oceanographic Research Papers*, *56*(1), 73–88. https://doi.org/10.1016/j.dsr.2008.08.003

Ito, T., & Follows, M. J. (2005). Preformed phosphate, soft tissue pump and atmospheric CO2. *Journal of*

Marine Research, *63*(4), 813–839. https://doi.org/10.1357/0022240054663231
Karl, D. M., Knauer, G. A., & Martin, J. H. (1988). Downward flux of particulate organic matter in the ocean: a particle decomposition paradox. *Nature*, *332*(6163), 438–441. https://doi.org/10.1038/332438a0
Karl, D. M., Christian, J. R., Dore, J. E., Hebel, D. V., Letelier, R. M., Tupas, L. M., & Winn, C. D. (1996). Seasonal and interannual variability in primary production and particle flux at Station ALOHA. *Deep Sea Research Part II: Topical Studies in Oceanography*, *43*(2–3), 539–568. https://doi.org/10.1016/0967-0645(96)00002-1
Karl, D. M., Church, M. J., Dore, J. E., Letelier, R. M., & Mahaffey, C. (2012). Predictable and efficient carbon sequestration in the North Pacific Ocean supported by symbiotic nitrogen fixation. *Proceedings of the National Academy of Sciences of the United States of America*, *109*(6), 1842–1849. https://doi.org/10.1073/pnas.1120312109
Khatiwala, S. (2007). A computational framework for simulation of biogeochemical tracers in the ocean. *Global Biogeochemical Cycles*, *21*(3). https://doi.org/10.1029/2007GB002923
Khatiwala, S., Visbeck, M., & Cane, M. A. (2005). Accelerated simulation of passive tracers in ocean circulation models. *Ocean Modelling*, *9*(1), 51–69. https://doi.org/10.1016/j.ocemod.2004.04.002
Khatiwala, S., Primeau, F. W., & Holzer, M. (2012). Ventilation of the deep ocean constrained with tracer observations and implications for radiocarbon estimates of ideal mean age. *Earth and Planetary Science Letters*, *325–326*, 116–125. https://doi.org/10.1016/j.epsl.2012.01.038
Khatiwala, S., Schmittner, A., & Muglia, J. (2019). Air-sea disequilibrium enhances ocean carbon storage during glacial periods. *Science Advances*, *5*(6), 1–11. https://doi.org/10.1126/sciadv.aaw4981
Knauer, G. A., Martin, J. H., & Bruland, K. W. (1979). Fluxes of particulate carbon, nitrogen, and phosphorus in the upper water column of the northeast Pacific. *Deep Sea Research Part A. Oceanographic Research Papers*, *26*(1), 97–108. https://doi.org/10.1016/0198-0149(79)90089-X
Kriest, I., & Oschlies, A. (2013). Swept under the carpet: Organic matter burial decreases global ocean biogeochemical model sensitivity to remineralization length scale. *Biogeosciences*, *10*(12), 8401–8422. https://doi.org/10.5194/bg-10-8401-2013
Kriest, I., & Oschlies, A. (2015). MOPS-1.0: Towards a model for the regulation of the global oceanic nitrogen budget by marine biogeochemical processes. *Geoscientific Model Development*, *8*(9), 2929–2957. https://doi.org/10.5194/gmd-8-2929-2015
Kriest, I., Kähler, P., Koeve, W., Kvale, K. F., Sauerland, V., & Oschlies, A. (2020). One size fits all? Calibrating an ocean biogeochemistry model for different circulations. *Biogeosciences*, *17*(12), 3057–3082. https://doi.org/10.5194/bg-17-3057-2020
Kwiatkowski, L., Aumont, O., Bopp, L., & Ciais, P. (2018). The Impact of Variable Phytoplankton Stoichiometry on Projections of Primary Production, Food Quality, and Carbon Uptake in the Global Ocean. *Global Biogeochemical Cycles*, *32*(4), 516–528. https://doi.org/10.1002/2017GB005799
Kwon, E. Y., Primeau, F. W., & Sarmiento, J. L. (2009). The impact of remineralization depth on the air-sea carbon balance. *Nature Geoscience*, *2*(9), 630–635. https://doi.org/10.1038/ngeo612
Lamborg, C. H., Buesseler, K. O., Valdes, J., Bertrand, C. H., Bidigare, R., Manganini, S., et al. (2008). The flux of bio- and lithogenic material associated with sinking particles in the mesopelagic "twilight zone" of the northwest and North Central Pacific Ocean. *Deep Sea Research Part II: Topical Studies in Oceanography*, *55*(14–15), 1540–1563. https://doi.org/10.1016/j.dsr2.2008.04.011
Lauderdale, J. M., & Cael, B. B. (2021). Impact of Remineralization Profile Shape on the Air-Sea Carbon Balance. *Geophysical Research Letters*, *48*(7), e2020GL091746. https://doi.org/10.1029/2020GL091746
Loh, A. N., & Bauer, J. E. (2000). Distribution, partitioning and fluxes of dissolved and particulate organic C, N and P in the eastern North Pacific and Southern Oceans. *Deep Sea Research Part I: Oceanographic Research Papers*, *47*(12), 2287–2316. https://doi.org/10.1016/S0967-0637(00)00027-3

Lomas, M. W., Burke, A. L., Lomas, D. A., Bell, D. W., Shen, C., Dyhrman, S. T., & Ammerman, J. W. (2010). Sargasso Sea phosphorus biogeochemistry: An important role for dissolved organic phosphorus (DOP). *Biogeosciences*, *7*(2), 695–710. https://doi.org/10.5194/bg-7-695-2010

Marinov, I., Follows, M. J., Gnanadesikan, A., Sarmiento, J. L., & Slater, R. D. (2008). How does ocean biology affect atmospheric p CO 2 ? Theory and models. *Journal of Geophysical Research*, *113*(C7), C07032. https://doi.org/10.1029/2007JC004598

Marinov, I., Gnanadesikan, A., Sarmiento, J. L., Toggweiler, J. R., Follows, M., & Mignone, B. K. (2008). Impact of oceanic circulation on biological carbon storage in the ocean and atmospheric p CO 2. *Global Biogeochemical Cycles*, *22*(3), n/a-n/a. https://doi.org/10.1029/2007GB002958

Martin, A., Boyd, P. W., Buesseler, K., Cetinic, I., Claustre, H., Giering, S., et al. (2020). The oceans' twilight zone must be studied now, before it is too late. *Nature*, *580*(7801), 26–28. https://doi.org/10.1038/d41586-020-00915-7

Martin, J. H., Knauer, G. A., Karl, D. M., & Broenkow, W. W. (1987). VERTEX: carbon cycling in the northeast Pacific. *Deep Sea Research Part A. Oceanographic Research Papers*, *34*(2), 267–285. https://doi.org/10.1016/0198-0149(87)90086-0

Martiny, A. C., Pham, C. T. A., Primeau, F. W., Vrugt, J. A., Moore, J. K., Levin, S. A., & Lomas, M. W. (2013). Strong latitudinal patterns in the elemental ratios of marine plankton and organic matter. *Nature Geoscience*, *6*(4), 279–283. https://doi.org/10.1038/ngeo1757

Martiny, A. C., Vrugt, J. A., & Lomas, M. W. (2014). Concentrations and ratios of particulate organic carbon, nitrogen, and phosphorus in the global ocean. *Scientific Data*, *1*, 140048. https://doi.org/10.1038/sdata.2014.48

Matsumoto, K. (2007). Biology-mediated temperature control on atmospheric pCO2 and ocean biogeochemistry. *Geophysical Research Letters*, *34*(20), 1–5. https://doi.org/10.1029/2007GL031301

Matsumoto, K., Tanioka, T., & Zahn, J. (2021). MESMO 3: Flexible phytoplankton stoichiometry and refractory dissolved organic matter. *Geoscientific Model Development*, *14*(4), 2265–2288. https://doi.org/10.5194/gmd-14-2265-2021

Menzel, D. W., & Ryther, J. H. (1964). The Composition of Particulate Organic Matter in the Western North Atlantic. *Limnology and Oceanography*, *9*(2), 179–186. https://doi.org/10.4319/lo.1964.9.2.0179

Minster, J. F., & Boulahdid, M. (1987). Redfield ratios along isopycnal surfaces-a complementary study. *Deep Sea Research Part A, Oceanographic Research Papers*, *34*(12), 1981–2003. https://doi.org/10.1016/0198-0149(87)90094-X

Pahlow, M., Chien, C.-T., Arteaga, L. A., & Oschlies, A. (2020). Optimality-based non-Redfield plankton-ecosystem model (OPEM v1.1) in UVic-ESCM 2.9 - Part 1: Implementation and model behaviour. *Geoscientific Model Development*, *13*(10), 4663–4690. https://doi.org/10.5194/gmd-13-4663-2020

Pavia, F. J., Anderson, R. F., Lam, P. J., Cael, B. B., Vivancos, S. M., Fleisher, M. Q., et al. (2019). Shallow particulate organic carbon regeneration in the South Pacific Ocean. *Proceedings of the National Academy of Sciences of the United States of America*, *116*(20), 9753–9758. https://doi.org/10.1073/pnas.1901863116

Paytan, A., Cade-Menun, B. J., McLaughlin, K., & Faul, K. L. (2003). Selective phosphorus regeneration of sinking marine particles: evidence from 31P-NMR. *Marine Chemistry*, *82*(1–2), 55–70. https://doi.org/10.1016/S0304-4203(03)00052-5

R Core Team. (2021). R: A Language and Environment for Statistical Computing. Vienna, Austria. Retrieved from https://www.r-project.org/

Robinson, C., Steinberg, D. K., Anderson, T. R., Arístegui, J., Carlson, C. A., Frost, J. R., et al. (2010). Mesopelagic zone ecology and biogeochemistry – a synthesis. *Deep Sea Research Part II: Topical Studies in Oceanography*, *57*(16), 1504–1518. https://doi.org/10.1016/j.dsr2.2010.02.018

Saba, G. K., Burd, A. B., Dunne, J. P., Hernández-León, S., Martin, A. H., Rose, K. A., et al. (2021). Toward a better understanding of fish-based contribution to ocean carbon flux. *Limnology and Oceanography*, *66*(5), 1639–1664. https://doi.org/10.1002/lno.11709

Sarmiento, J. L., & Toggweiler, J. R. (1984). A new model for the role of the oceans in determining atmospheric PCO2. *Nature*, *308*(5960), 621–624. https://doi.org/10.1038/308621a0

Schiettekatte, N. M. D., Barneche, D. R., Villéger, S., Allgeier, J. E., Burkepile, D. E., Brandl, S. J., et al. (2020). Nutrient limitation, bioenergetics and stoichiometry: A new model to predict elemental fluxes mediated by fishes. *Functional Ecology*, *34*(9), 1857–1869. https://doi.org/10.1111/1365-2435.13618

Shaffer, G., Bendtsen, J., & Ulloa, O. (1999). Fractionation during remineralization of organic matter in the ocean. *Deep-Sea Research Part I: Oceanographic Research Papers*, *46*(2), 185–204. https://doi.org/10.1016/S0967-0637(98)00061-2

Sigman, D. M., & Boyle, E. A. (2000). Glacial/interglacial variations in atmospheric carbon dioxide. *Nature*, *407*(6806), 859–869. https://doi.org/10.1038/35038000

Stammer, D., Ueyoshi, K., Köhl, A., Large, W. G., Josey, S. A., & Wunsch, C. (2004). Estimating air-sea fluxes of heat, freshwater, and momentum through global ocean data assimilation. *Journal of Geophysical Research C: Oceans*, *109*(5), C05023. https://doi.org/10.1029/2003JC002082

Steinberg, D. K., & Landry, M. R. (2017). Zooplankton and the Ocean Carbon Cycle. *Annual Review of Marine Science*, (October 2016), 1–32. https://doi.org/10.1146/annurev-marine-010814-015924

Tanioka, T., & Matsumoto, K. (2017). Buffering of Ocean Export Production by Flexible Elemental Stoichiometry of Particulate Organic Matter. *Global Biogeochemical Cycles*, *31*(10), 1528–1542. https://doi.org/10.1002/2017GB005670

Tanioka, T., & Matsumoto, K. (2020). A meta-analysis on environmental drivers of marine phytoplankton C : N : P. *Biogeosciences*, *17*(11), 2939–2954. https://doi.org/10.5194/bg-17-2939-2020

Taylor, G., Karl, D. M., & Pace, M. (1986). Impact of bacteria and zooflagellates on the composition of sinking particles: an in situ experiment. *Marine Ecology Progress Series*, *29*, 141–155. https://doi.org/10.3354/meps029141

Teng, Y.-C., Primeau, F. W., Moore, J. K., Lomas, M. W., & Martiny, A. C. (2014). Global-scale variations of the ratios of carbon to phosphorus in exported marine organic matter. *Nature Geoscience*, *7*(12), 895–898. https://doi.org/10.1038/ngeo2303

Wakeham, S. G., Lee, C., Farrington, J. W., & Gagosian, R. B. (1984). Biogeochemistry of particulate organic matter in the oceans: results from sediment trap experiments. *Deep Sea Research Part A. Oceanographic Research Papers*, *31*(5), 509–528. https://doi.org/10.1016/0198-0149(84)90099-2

Weber, T. S., & Deutsch, C. (2010). Ocean nutrient ratios governed by plankton biogeography. *Nature*, *467*(7315), 550–554. https://doi.org/10.1038/nature09403

Figures

Figure 1. Depth profiles of C:P of sinking POM from our new data compilation. (a) Locations of samples collected shown with red crosses superimposed on the modeled C:P of suspended POM at the surface. The boundaries are based on the 0.3 mmol m^{-3} of the annually averaged surface PO_4 concentration. (b) Depth profile of C:P flux ratio of sinking POM (red cross) with C:P of suspended POM in the top 300 m (blue circle; Martiny et al., 2013). C:P flux ratios from a 3D model with different values of b_C (Martin *b* of POC) are shown with black dotted lines. Only the values between 100 and 2000 m are shown here.

Figure 2. Martin *b* estimated from particulate sedimentary flux profiles at BATS. (a) Time-series of the Martin *b* parameters from 2006 to 2019 for Particulate Phosphorus, PP (b_P, red) and Particulate Organic Carbon, POC (b_C, blue). Smooth lines are Locally Weighted Least Squares Regression. (b) Violin plot for average Martin *b* values at BATS from 2006 to 2019. The whiskers of the box plot cover 95% confidence interval, and the box shows 25%, 50%, and 75% percentiles. The median values of b_P *and* b_C are 1.28 and 0.98, respectively.

Figure 3. Comparing model and theoretical prediction on the influence of $r_{C:P}$ on ocean carbon storage at steady state. The relationship between $r_{C:P}$ and (a) ocean carbon storage due to soft-tissue pump and (b) atmospheric CO_2. In both panels, model results are shown with dots, and theoretical predictions with different twilight zone depth range z' are shown with black lines. The color for plots indicates different Martin *b* parameters for POC used in the simulations. Also shown are threshold OCS_{soft} and pCO_2 when the entire phosphate is in the regenerated form under fixed $r_{C:P}$ of 117.

Figure 1.

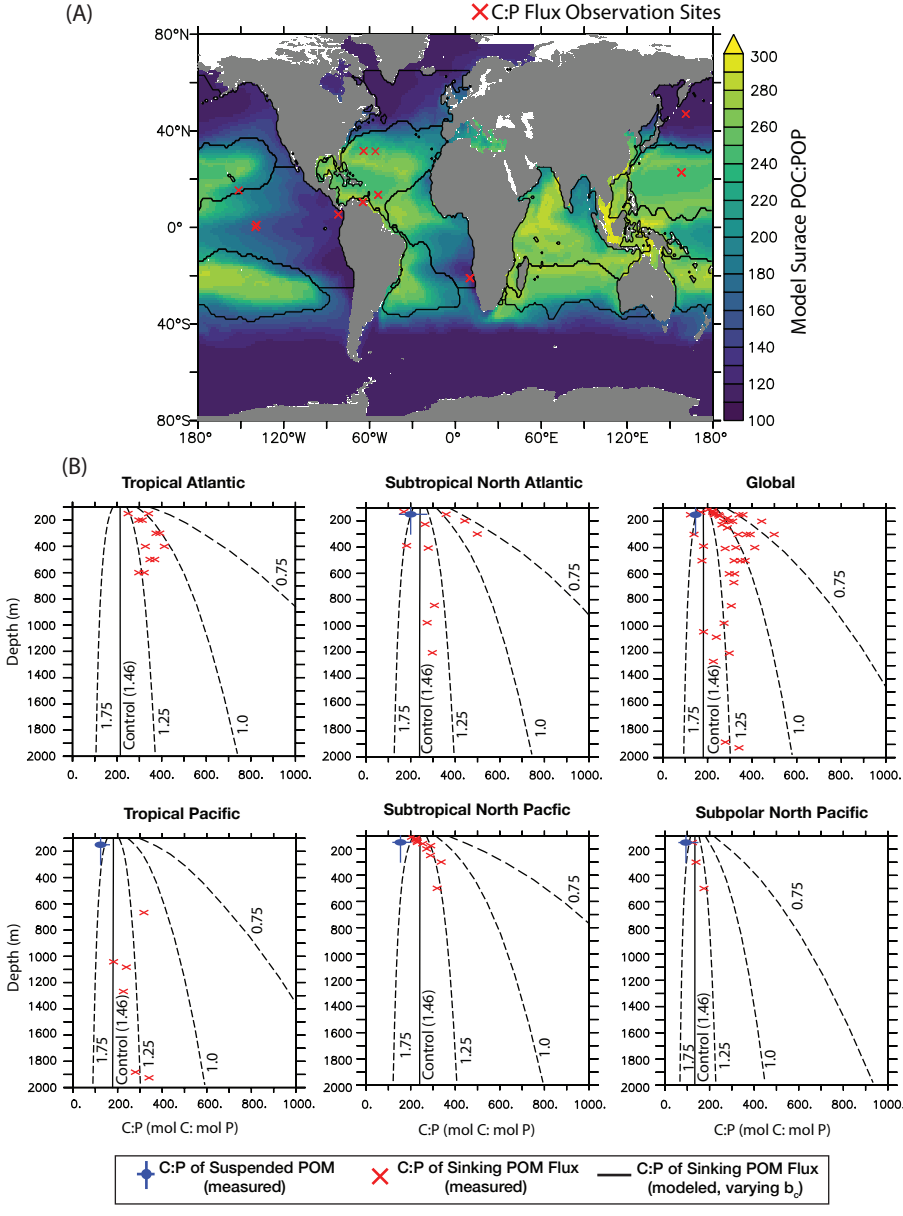
(A)
C:P Flux Observation Sites
80°N
40°N
0°
40°S
80°S
180°
120°W
60°W
0°
60°E
120°E
180°
300
280
260
240
220
200
180
160
140
120
100
Model Surace POC:POP
(B)
Tropical Atlantic
Subtropical North Atlantic
Global
Tropical Pacific
Subtropical North Pacfic
Subpolar North Pacific
Depth (m)
200
400
600
800
1000
1200
1400
1600
1800
2000
0.
200.
400.
600.
800.
1000.
1.75
Control (1.46)
1.25
1.0
0.75
C:P (mol C: mol P)
C:P of Suspended POM (measured)
C:P of Sinking POM Flux (measured)
C:P of Sinking POM Flux (modeled, varying b$_o$)

Figure 2.

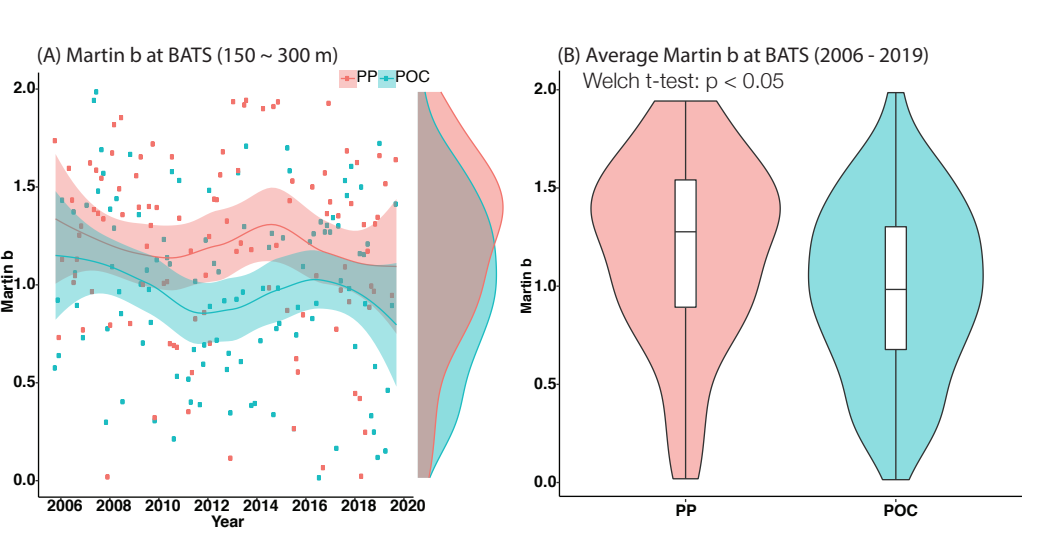
(A) Martin b at BATS (150 ~ 300 m)
PP
POC
Martin b
2.0
1.5
1.0
0.5
0.0
2006
2008
2010
2012
2014
2016
2018
2020
Year
(B) Average Martin b at BATS (2006 - 2019)
Welch t-test: p < 0.05
Martin b
2.0
1.5
1.0
0.5
0.0
PP
POC

Figure 3.

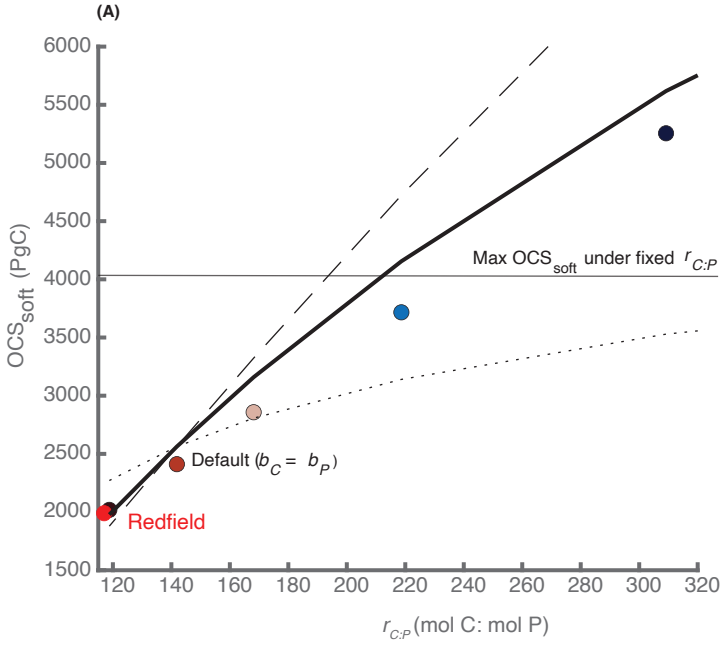
(A)
6000
5500
5000
4500
4000
3500
3000
2500
2000
1500
OCS soft (PgC)
Max OCS soft under fixed r C:P
Default (b C = b P)
Redfield
120
140
160
180
200
220
240
260
280
300
320
r C:P (mol C: mol P)

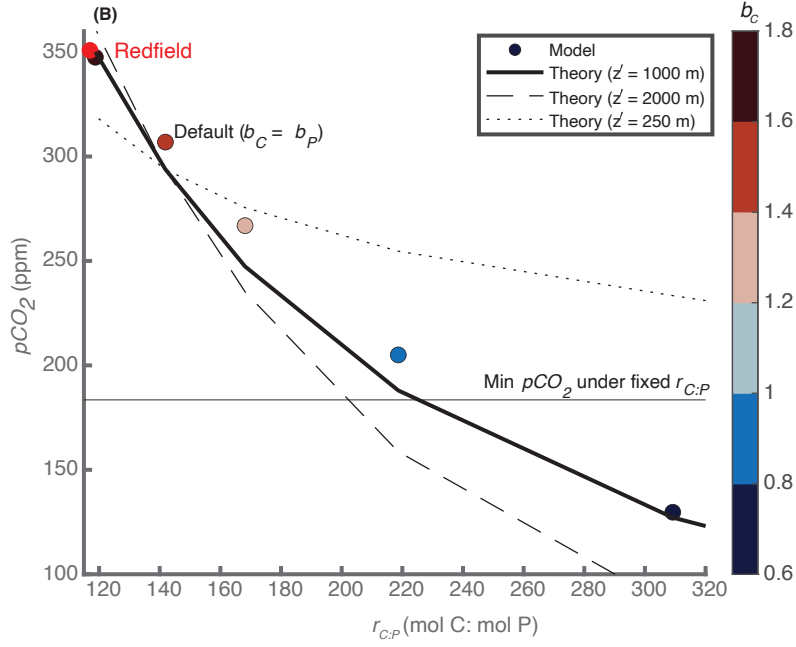
(B)
Redfield
Default (b C = b P)
Model
Theory (z′ = 1000 m)
Theory (z′ = 2000 m)
Theory (z′ = 250 m)
Min pCO 2 under fixed r C:P
pCO 2 (ppm)
350
300
250
200
150
100
120
140
160
180
200
220
240
260
280
300
320
r C:P (mol C: mol P)
b C
1.8
1.6
1.4
1.2
1
0.8
0.6

Geophysical Research Letters

Supporting Information for

Drawdown of Atmospheric pCO_2 via Variable Particle Flux Stoichiometry in the Ocean Twilight Zone

Tatsuro Tanioka[1,2,*], Katsumi Matsumoto[1], and Michael W. Lomas[3]

[1] Department of Earth & Environmental Sciences, University of Minnesota, Minneapolis, MN, USA

[2] Department of Earth System Science, University of California Irvine, Irvine, CA, USA

[3] Bigelow Laboratory for Ocean Sciences, East Boothbay, ME, USA

**Correspondence to*: Tatsuro Tanioka (tatsurt@uci.edu)

Contents of this file

Introduction

This Supplementary Information contains POC:POP flux measurements used in Figure 1 (separate file), model description, model parameters, and model results. Model codes are archived in the Zenodo (https://doi.org/10.5281/zenodo.4960404) and model input/output are publicly archived in Dryad (https://doi.org/10.5061/dryad.70rxwdbx).

Text S1: Model Equations for Biogeochemical model MOPS

S1.1 Source-minus-sink terms in MOPS (see Kriest and Oschlies, 2015 for full details)

9 state variables are: PO_4, phytoplankton biomass in P (PHY), zooplankton biomass in P (ZOO), dissolved organic phosphorus (DOP), particulate organic phosphorus (POP), dissolved O_2, NO_3, DIC, and alkalinity (constant). Notations and parameters follow the original model description paper (Kriest & Oschlies, 2015) except for POP, which is denoted as "Detritus (DET)" in the original paper. In the original model, C:P for phytoplankton ($r_{C:P}^{PHY}$) and zooplankton ($r_{C:P}^{ZOO}$) are fixed at 117:1.

$$S(PO_4) = (-PP + \lambda_{ZOO} ZOO)\mathcal{H}_e(k) + S_{PO_4}^R + S_{PO_4}^D \quad (1)$$

$$S(PHY) = (PP - G - \lambda_{PHY} PHY)\mathcal{H}_e(k) - S_{PHY}^M \quad (2)$$

$$S(ZOO) = (\epsilon_{ZOO} G - \lambda_{ZOO} ZOO - \kappa_{ZOO} ZOO^2)\mathcal{H}_e(k) - S_{ZOO}^M \quad (3)$$

$$S(DOP) = \sigma_{DOP}[(1 - \epsilon_{ZOO})G + \kappa_{ZOO} ZOO^2 + \lambda_{PHY} PHY]\mathcal{H}_e(k) + S_{PHY}^M + S_{ZOO}^M - S_{DOP}^R - S_{DOP}^D \quad (4)$$

$$S(POP) = (1 - \sigma_{DOP})[(1 - \epsilon_{ZOO})G + \kappa_{ZOO} ZOO^2 + \lambda_{PHY} PHY]\mathcal{H}_e(k) - S_{POP}^R - S_{POP}^D + \frac{\partial w POP^*}{\partial z}$$

$$POP^* = \max(0, POP - P_{min}) \quad (5)$$

$$S(O_2) = R_{-O_2:P}(PP - \lambda_{ZOO} ZOO)\mathcal{H}_e(k) - S_{O_2}^R \quad (6)$$

$$S(NO_3) = d(-PP + \lambda_{ZOO} ZOO)\mathcal{H}_e(k) + S_{NO_3}^{NFix} + S_{NO_3}^R - S_{NO_3}^D \quad (7)$$

$$S(DIC) = (-PP \cdot r_{C:P}^{PHY} + \lambda_{ZOO} ZOO \cdot r_{C:P}^{ZOO})\mathcal{H}_e(k) + S_{DIC}^R + S_{DIC}^D \quad (8)$$

S1.2. New source-minus-sink terms for organic carbon state variables

We added 4 new state variables related to organic carbon: phytoplankton biomass in C (PHY_C), zooplankton biomass in C (ZOO_C), dissolved organic carbon C (DOC), and particulate organic carbon (POC). Kinetic parameters such as rate constants (λ) for remineralization for various source-minus-sink terms of POC and DOC are identical to those of POP and DOP, respectively. Details on computing phytoplankton C:P ratio ($r_{C:P}^{PHY}$) and zooplankton C:P ratio ($r_{C:P}^{ZOO}$) are described in the main text.

$$S(PHY_C) = S(PHY) \cdot r_{C:P}^{PHY} \quad (9)$$

$$S(ZOO_C) = (\epsilon_{ZOO} G \cdot r_{C:P}^{PHY} - \lambda_{ZOO} ZOO \cdot r_{C:P}^{ZOO} - \kappa_{ZOO} ZOO^2 \cdot r_{C:P}^{ZOO}) \mathcal{H}_e(k) - S_{ZOO}^M \cdot r_{C:P}^{ZOO} \quad (10)$$

$$S(DOC) = \sigma_{DOP}[(1-\epsilon_{ZOO}) G \cdot r_{C:P}^{PHY} + \kappa_{ZOO} ZOO^2 \cdot r_{C:P}^{ZOO} + \lambda_{PHY} PHY \cdot r_{C:P}^{PHY}] \mathcal{H}_e(k) + S_{PHY}^M \cdot r_{C:P}^{PHY} + S_{ZOO}^M \cdot r_{C:P}^{ZOO} - S_{DOC}^R - S_{DOC}^D \quad (11)$$

$$S(DET_C) = (1-\sigma_{DOP})[(1-\epsilon_{ZOO}) G \cdot r_{C:P}^{PHY} + \kappa_{ZOO} ZOO^2 \cdot r_{C:P}^{ZOO} + \lambda_{PHY} PHY \cdot r_{C:P}^{PHY}] \mathcal{H}_e(k) - S_{POC}^R - S_{POC}^D + \frac{\partial w POC^*}{\partial z}$$

$$POC^* = \max(0, POC^* - P_{min} \times 117) \quad (12)$$

$$r_{C:P}^{PHY} = \frac{1}{[P:C]_{PHY}} = 1/[P:C]_{PHY,ref} \cdot \left(\frac{[PO_4]}{[PO_4]_0}\right)^{s_{PO_4}^{P:C}} \cdot \left(\frac{T}{T_0}\right)^{s_T^{P:C}} \quad (13)$$

$$r_{C:P}^{ZOO} = \frac{1}{[P:C]_{ZOO}} = 1/[P:C]_{zoo,ref}{}^{1-H} [P:C]_{PHY}{}^{H} \quad (14)$$

S1.3. Release of excess C or P by zooplankton for maintaining homeostatic C:P

When phytoplankton C:P does not equal C:P of zooplankton, zooplankton needs to release extra C or P from uptake into the particulate organic matter pool for zooplankton to maintain their homeostatic C:P. When phytoplankton $r_{C:P}^{PHY}$ is greater than $r_{C:P}^{ZOO}$ (i.e., excess C), extra C is added back to POC. The flux of excess C released E_{ZOO}^C is,

$$E_{ZOO}^C = \epsilon_{ZOO} G \times \max(0, r_{C:P}^{PHY} - r_{C:P}^{ZOO}) \quad (15)$$

The updated SMS terms for zooplankton carbon biomass and POC are:
$S(ZOO_C)^* = S(ZOO_C) - E_{ZOO}^C$

$$S(ZOO_C)^* = \text{Updated SMS of } \mathrm{ZOO_C} \text{ after zooplankton C release} \quad (16)$$

$S(POC)^* = S(POC) + E_{ZOO}^C$

$$S(POC)^* = \text{Updated SMS of POC after zooplankton C release} \quad (17)$$

Conversely, if phytoplankton $r_{C:P}^{PHY}$ is less than $r_{C:P}^{ZOO}$ (i.e., excess P), zooplankton releases its extra P back to POP. The flux of extra P (E_{ZOO}^P):

$$E_{ZOO}^{P} = \epsilon_{ZOO} G \times \max\left(0, 1 - \frac{r_{C:P}^{PHY}}{r_{C:P}^{ZOO}}\right) \quad (18)$$

The updated SMS terms for zooplankton biomass in P and POP are:

$$S(ZOO)^{*} = S(ZOO) - E_{ZOO}^{P}$$

$$S(ZOO)^{*} = \text{Updated SMS of ZOO after zooplankton P release} \quad (19)$$

$$S(POP)^{*} = S(POP) + E_{ZOO}^{P}$$

$$S(POP)^{*} = \text{Updated SMS of POP ater zooplankton P release} \quad (20)$$

With this flux adjustment, $S(ZOO_C)^{*} = S(ZOO)^{*} \cdot r_{C:P}^{ZOO}$ and it ensures the total mass of C and P in the system are conserved.

In our sensitivity runs, we set a hard-bound minimum on C:P of phytoplankton so that $r_{C:P}^{PHY}$ is always greater than or equal to $r_{C:P}^{ZOO}$. This way, zooplankton do not excrete excess P into POP, which keeps phosphate distribution identical in each sensitivity run.

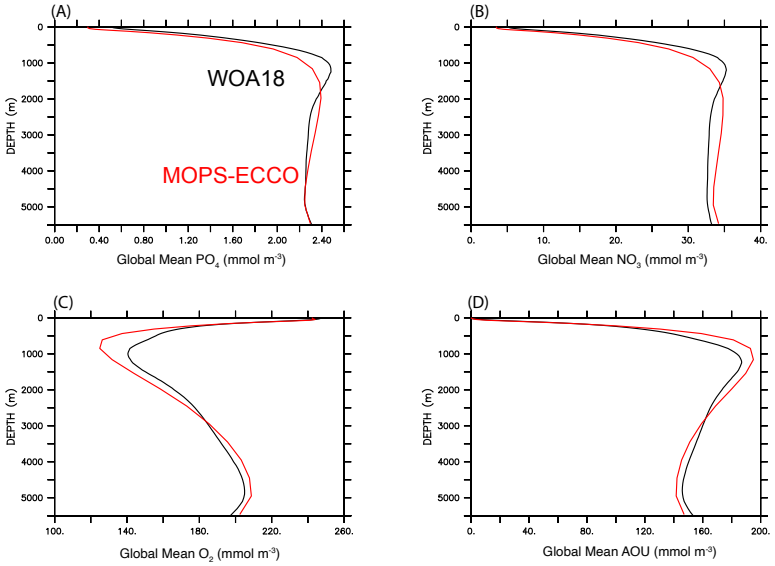

Figure S1. Global mean vertical profiles of phosphate (a), nitrate (b), oxygen (c), and AOU (d). Red lines are model outputs after 3000 years of spin-up, and black lines are observations from World Ocean Atlas 2018 (Garcia et al., 2018).

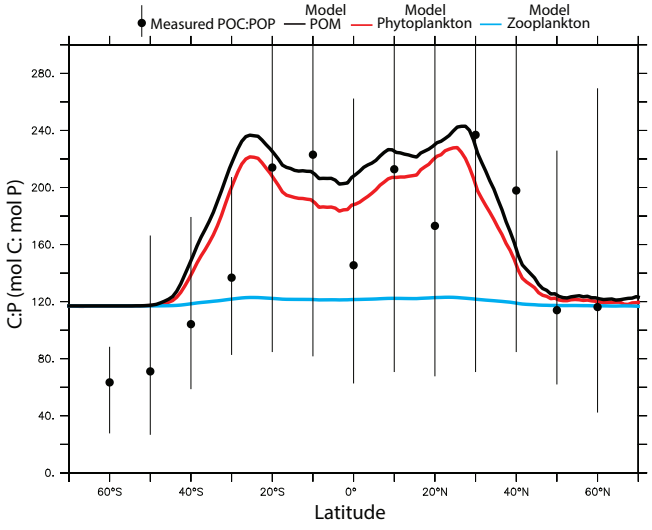

Figure S2. Zonal mean C:P of model suspended POM (black), phytoplankton (red), and zooplankton (blue) in the surface ocean after 3000 years of spin-up. Black boxes show median and the 95% confidence interval of observed suspended C:P of POM binned by latitude (Martiny et al., 2013).

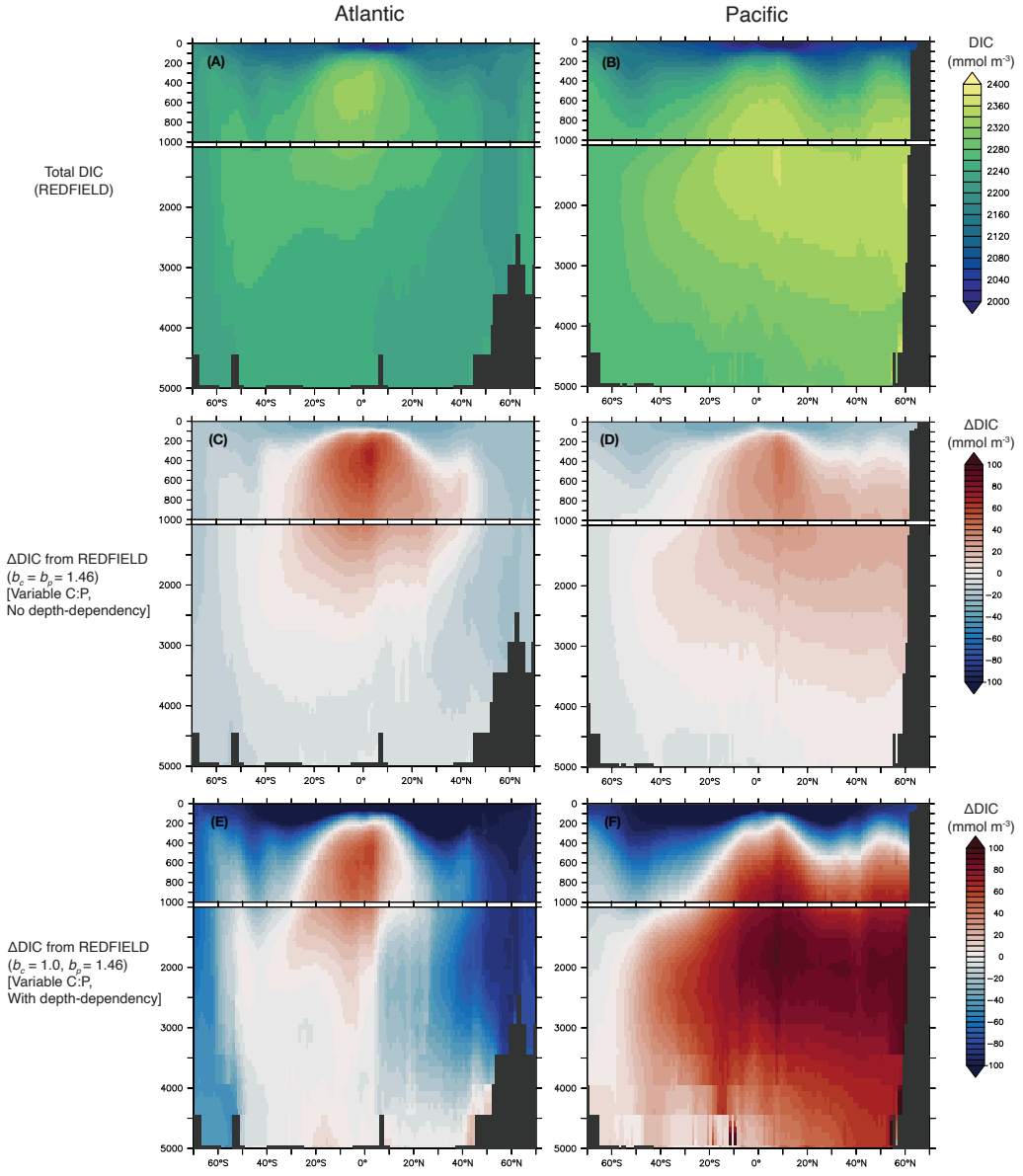

Figure S3. Zonal-averaged DIC under the Redfield run with fixed C:P, and no preferential remineralization (a-b), DIC anomaly (ΔDIC) from the Redfield run in the control run without preferential remineralization (c-d), and in a run with preferential remineralization of POP over POC (e-f).

Table S1. List of POC:POP flux measurements. Abbreviations: TA = Tropic Atlantic, TP = Tropical Pacific, STNA = Subtropical North Atlantic, STNP = Subtropical North Pacific, SNP = Subpolar North Pacific.

Table S2. Median C:P of suspended POM and sinking POM from different oceanographic regions and with different sediment trap types delineated by depth. Brackets indicate the number of samples.

Regions	**C:P of Suspended POM* (top 300 m)**	**C:P Flux Ratio**		
		Twilight Zone (100 - 1000 m)	Deep (> 1000 m)	All
Tropical Atlantic	-	334 (12)	-	334 (12)
Tropical Pacific	124	318 (1)	267 (11)	274 (12)
Subtropical North Atlantic	200	279 (9)	191 (4)	274 (13)
Subtropical North Pacific	154	254 (11)	243 (3)	248 (14)
Subpolar North Pacific	94	142 (3)		142 (3)
Global	146	294 (36)	243 (18)	273 (54)
Sediment Trap Types				
Moored	N/A	274 (7)	243 (18)	265 (25)
Surface tethered		316 (26)	-	316 (26)
Free-drifting		142 (3)	-	142 (3)

* Median C:P of suspended POM from Martiny et al. (2014)

Table S3. Summary of analysis of variance (ANOVA). Log-transformed C:P flux ratio was analyzed on a two-factorial ANOVA, using region and depth (twilight zone or deep) as independent factors and C:P flux ratios as the dependent variable. Asterisk (*) signifies statistical significance ($p < 0.05$).

Factor	MS	df	*F*	*p*
Region	0.4505	4	7.633	8.37e-5*
Depth	0.3683	1	6.249	0.0161*
Region x Depth	0.1289	2	2.184	0.1241
Residuals	0.0590	46		

Table S4. Summary of BATS timeseries analysis.

Martin curve parameter	**n**	**Median**	**t-test**
b_P (PP)	106	1.28	p = 0.0015
b_C (POC)	111	0.98	(p < 0.05)

Table S5. Summary of BATS timeseries analysis. The key biogeochemical parameters, including the Martin b for POP, were objectively calibrated specifically for the ECCO transport matrix field to match observed PO_4, O_2, and NO_3 (Kriest et al., 2020; Figure S1). Phytoplankton power law parameter values for P:C ($\boldsymbol{s_{PO_4}^{P:C}}$ and $\boldsymbol{s_T^{P:C}}$) are weighted-mean values across all phytoplankton types based on meta-analysis of Tanioka & Matsumoto (2020) (their Table 2).

Parameter	**Description**	**Unit**	**Value**
Calibrated Parameters from Kriest et al. 2020 for MOPS + ECCO TMs			
b (= b_P)	Martin b for POP	-	1.46
$R_{-O_2:P}$	$-O_2:P$ of remineralization	mol: mol	151.1
μ_{NFix}	Maximum nitrogen fixation rate	d^{-1}	2.29
DIN_{min}	Threshold nitrate concentration for denitrification	mmol m^{-3}	16.0
K_{DIN}	Half-saturation constant for nitrate	mmol m^{-3}	23.1
K_{O_2}	Half-saturation constant for aerobic remineralization	mmol m^{-3}	1.07
Parameters for new organic carbon module			
b_C	Martin b for POC	-	Variable (Control = 1.46)
$[P:C]_{PHY,ref}$	Reference P:C molar ratio of phytoplankton	mol: mol	1/117
$[P:C]_{zoo,ref}$	Reference P:C molar ratio of zooplankton	mol: mol	1/117
$[PO_4]_0$	Reference PO_4	mmol m^{-3}	0.57
T_0	Reference T	◦K	291
$s_{PO_4}^{P:C}$	Sensitivity of phytoplankton P:C to PO_4	-	0.21
$s_T^{P:C}$	Sensitivity of phytoplankton P:C to T	-	-3.6
H	Homeostatic parameter of zooplankton	-	0.08

Table S6. Summary of sensitivity model run results with varying Martin *b* for POC (b_C). Martin *b* for POP (b_P) is constant at 1.46 in all runs. All sensitivity experiments are conducted for 1000 years following 3000 years of the spin-up run.

Run ID	**Gas exchange**	**C:P**	b_c	b_p	$r_{C:P}$ **at 100 m (mol C:mol P)**	$r_{C:P}$ **(mol C:mol P)**	OCS_{soft} **(PgC)**	$C_{buffered}$ **(PgC)**	**Revelle Factor, R**	$V_{OC} \cdot \overline{DIC_{eq}}$ **(PgC)**	pCO_{2a} **(ppm)**	**POC export at 100 m (PgC yr^{-1})**
201203a (Control)	Regular	Variable	1.46	1.46	151	159	2701	3251	12.7	33811	277.8	9.5
201204r	Fast	Variable	0.75	1.46	151	309	5255	3439	10.0	31580	130.2	15.7
201204h	Fast		1	1.46	151	219	3717	3344	11.3	32958	205.2	13.2
201204q	Fast		1.25	1.46	151	168	2858	3263	12.5	33685	267.2	11.3
201204d (Default)	Fast		1.46	1.46	151	142	2412	3220	13.2	34046	307.2	10.1
201204p	Fast		1.75	1.46	151	119	2019	3186	14.0	34352	347.2	8.8
201204j	Fast	Fixed (Redfield)	1.46	1.46	117	117	1990	3184	14.1	34374	351.2	7.1

Table S1: List of POC:POP flux measurements.

#	Study	Longitude	Latitude	Regions[1]	Depth (m)	C:P flux xw (molar)	Sample size, n	Sediment trap type
1	Antia05	-81.88	5.35	ETP	667	318.0	NA	Moored
2	Antia05	-81.88	5.35	ETP	1268	226.0	NA	Moored
3	Antia05	-81.88	5.35	ETP	2700	210.0	NA	Moored
4	Antia05	-81.88	5.35	ETP	3700	243.0	NA	Moored
5	Antia05	-54.00	13.50	NASG	389	182.0	NA	Moored
6	Antia05	-54.00	13.50	NASG	976	274.0	NA	Moored
7	Antia05	-55.92	31.54	NASG	3694	104.0	NA	Moored
8	Antia05	-54.00	13.50	NASG	3755	180.0	NA	Moored
9	Antia05	-54.00	13.50	NASG	5068	202.0	NA	Moored
10	Antia05	-151.48	15.35	NPSG	2778	303.0	NA	Moored
11	Antia05	-151.48	15.35	NPSG	4280	243.0	NA	Moored
12	Antia05	-64.67	10.50	ETP	667	169.7	14	Moored
13	BenitezNelson07	-64.67	10.50	NASG	130	264.6	171	Moored
14	BenitezNelson07	-64.67	10.50	NASG	226	278.9	160	Moored
15	BenitezNelson07	-64.67	10.50	NASG	407	306.7	145	Moored
16	BenitezNelson07	-64.67	10.50	NASG	844	297.3	131	Moored
17	BenitezNelson07	10.00	-21.00	NASG	1205	249.4	3	Moored
18	Engel17	10.25	-21.00	ETA	150	341.2	3	Surface_tethered
19	Engel17	10.00	-21.00	ETA	150	313.0	3	Surface_tethered
20	Engel17	10.25	-21.00	ETA	200	297.4	3	Surface_tethered
21	Engel17	10.00	-21.00	ETA	200	374.6	3	Surface_tethered
22	Engel17	10.25	-21.00	ETA	300	391.5	3	Surface_tethered
23	Engel17	10.00	-21.00	ETA	300	411.8	3	Surface_tethered
24	Engel17	10.25	-21.00	ETA	400	326.8	3	Surface_tethered
25	Engel17	10.00	-21.00	ETA	400	368.8	3	Surface_tethered
26	Engel17	10.25	-21.00	ETA	500	347.5	3	Surface_tethered
27	Engel17	10.00	-21.00	ETA	500	321.7	3	Surface_tethered
28	Engel17	10.25	-21.00	ETA	600	297.2	3	Surface_tethered
29	Faul05	-139.70	0.09	ETP	1042	182.0	2	Moored
30	Faul05	-139.00	1.06	ETP	1083	240.0	2	Moored
31	Faul05	-139.00	1.06	ETP	1883	281.3	2	Moored

[1] TA = Tropic Atlantic, TP = Tropical Pacific, STNA = Subtropical North Atlantic, STNP = Subtropical North Pacific, SNP = Subpolar North Pacific

32	Faul05	-139.70	0.09	ETP	1926	341.0	2	Moored
33	Faul05	-139.00	1.06	ETP	2908	344.0	2	Moored
34	Faul05	-139.70	0.09	ETP	3650	343.0	2	Moored
35	Faul05	-139.00	1.06	ETP	4220	345.0	2	Moored
36	Faul05	-139.00	1.06	ETP	4390	267.0	2	Moored
37	Grabowski19	158.00	22.75	NPSG	110	204.0	8	Surface_tethered
38	Grabowski19	158.00	22.75	NPSG	120	223.0	8	Surface_tethered
39	Grabowski19	158.00	22.75	NPSG	130	223.0	8	Surface_tethered
40	Grabowski19	158.00	22.75	NPSG	140	229.0	8	Surface_tethered
41	Grabowski19	158.00	22.75	NPSG	150	230.0	8	Surface_tethered
42	Grabowski19	158.00	22.75	NPSG	160	254.0	8	Surface_tethered
43	Grabowski19	158.00	22.75	NPSG	175	290.0	8	Surface_tethered
44	Grabowski19	158.00	22.75	NPSG	200	272.0	8	Surface_tethered
45	Grabowski19	158.00	22.75	NPSG	250	289.0	8	Surface_tethered
46	Grabowski19	158.00	22.75	NPSG	300	337.0	8	Surface_tethered
47	Grabowski19	158.00	22.75	NPSG	500	319.0	8	Surface_tethered
48	Karl12	158.00	22.75	NPSG	4000	218.4	226	Moored
49	Lamborg08	161.00	47.00	NPA	150	128.8	3	Free_drifting
50	Lamborg08	161.00	47.00	NPA	300	141.7	2	Free_drifting
51	Lamborg08	161.00	47.00	NPA	500	175.7	2	Free_drifting
52	Lomas10	-64.17	31.67	NASG	150	359.0	6	Surface_tethered
53	Lomas10	-64.17	31.67	NASG	200	443.0	6	Surface_tethered
54	Lomas10	-64.17	31.67	NASG	300	499.0	6	Surface_tethered

2